ACS Energy LETTERS

http://pubs.acs.org/journal/aelccp

LETTER

Self-Heating Conductive Ceramic Composites for High Temperature Thermal Energy Storage

Lin Yang,[†] Peng Peng,[†] Nathaniel Weger,[†] Sean Mills, Clément Messeri, Akanksha K. Menon, Steven Zeltmann, Finn Babbe, Qiye Zheng, Chaochao Dun, Chuan Zhang, Jeffrey J. Urban, Andrew M. Minor, Ravi Prasher,* Hanna Breunig,* and Sean Lubner*

Cite This: *ACS Energy Lett.* 2025, 10, 1002−1012

Read Online

ACCESS | Metrics & More | Article Recommendations | Supporting Information

ABSTRACT: **The absence of affordable and deployable large-scale energy storage poses a major barrier to providing zero-emission energy on demand for societal decarbonization. High temperature thermal energy storage is one promising option with low cost and high scalability, but it is hindered by the inherent complexity of simultaneously satisfying all of the material requirements. Here we design a class of ceramic−carbon composites based on co-optimizing mechanical, electrical, and thermal properties. These composites demonstrate stability in soak-and-hold tests and direct self-heating up to 1,936 °C and 750 thermal cycles from 500 to 1,630 °C without degradation. This thermal performance derives from their composition and microstructural design as verified by in situ high-temperature transmission electron microscopy and X-ray diffraction. They offer both higher energy density and lower cost than conventional storage technologies with a projected system Levelized Cost of Storage below the U.S. Department of Energy's 2030 target 5 ¢/kWh (electric).**

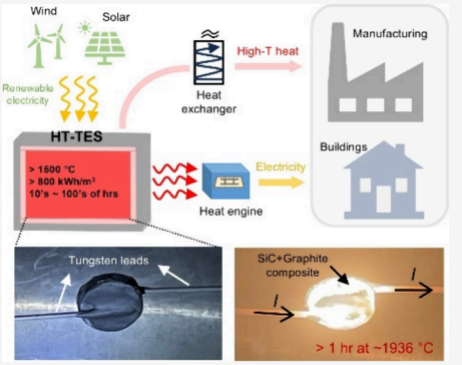

We will need Terawatt-hours of energy storage to overcome the intermittency of solar and wind power and fully transition to renewable energy.[1−4] Most existing energy storage technologies such as electrochemical batteries and pumped hydro are either too expensive for large scale deployment, geographically constrained,[2] or have critical material availability concerns.[3,4] Furthermore, a significant amount of end-use energy is needed as high temperature (>1,000 °C) thermal energy instead of electricity, especially for industrial processes such as steel, cement, and glass production.[5,6] We cannot achieve full decarbonization without also decarbonizing this high temperature industrial process heat.

Recently, high-temperature thermal energy storage (HT-TES) has emerged as a promising solution to these stated issues. These systems store renewable energy in the form of heat frequently above 1,500 °C and dispatch it either directly as heat or by converting it into electricity using a heat engine (also called Carnot batteries[7]) as shown in Figure 1a. HT-TES possesses several environmental and economic benefits that make it particularly well suited to TWh-scale deployment needed for full decarbonization, including high energy density (>800 kWh_{th}/m^3),[8,9] intrinsic safety (heat itself cannot explode), low capital cost (<US$10/kWh),[8,10] geographic flexibility, and reliance only on Earth abundant materials.[9−11] But the ideal HT-TES material must satisfy a challenging set of simultaneous constraints: good thermal conductivity to reduce temperature gradients and increase power delivery rates, good and temperature-independent electrical conductivity for rapid and stable self-heating, robust mechanical properties that withstand thermal shock and mitigate thermal cycling fatigue, high temperature stability, and noncorrosivity, all while being made from safe and abundant materials.

Scientists have investigated high temperature liquids for HT-TES such as molten silicon and tin,[12,13] as molten salts thermally degrade above 1,000 °C. However, containment of such high temperature corrosive liquids is difficult. Hexagonal boron nitride (h-BN),[14] its composites,[15,16] and graphite[12] have been explored as refractories for containment, among other materials. Each container material overcomes a key challenge, but no single material has yet eliminated mechanical weakness, degradation, chemical reactivity, and wettability with the corrosive liquid all at once. While phase change or sensible heat liquids hold promise for HT-TES, further advances in

Received: November 25, 2024
Revised: January 16, 2025
Accepted: January 23, 2025
Published: January 27, 2025

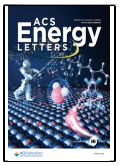

Downloaded via UNIV OF COLORADO BOULDER on February 19, 2025 at 23:13:38 (UTC).
See https://pubs.acs.org/sharingguidelines for options on how to legitimately share published articles.

ACS Publications © 2025 American Chemical Society

https://doi.org/10.1021/acsenergylett.4c03270
ACS Energy Lett. 2025, 10, 1002−1012

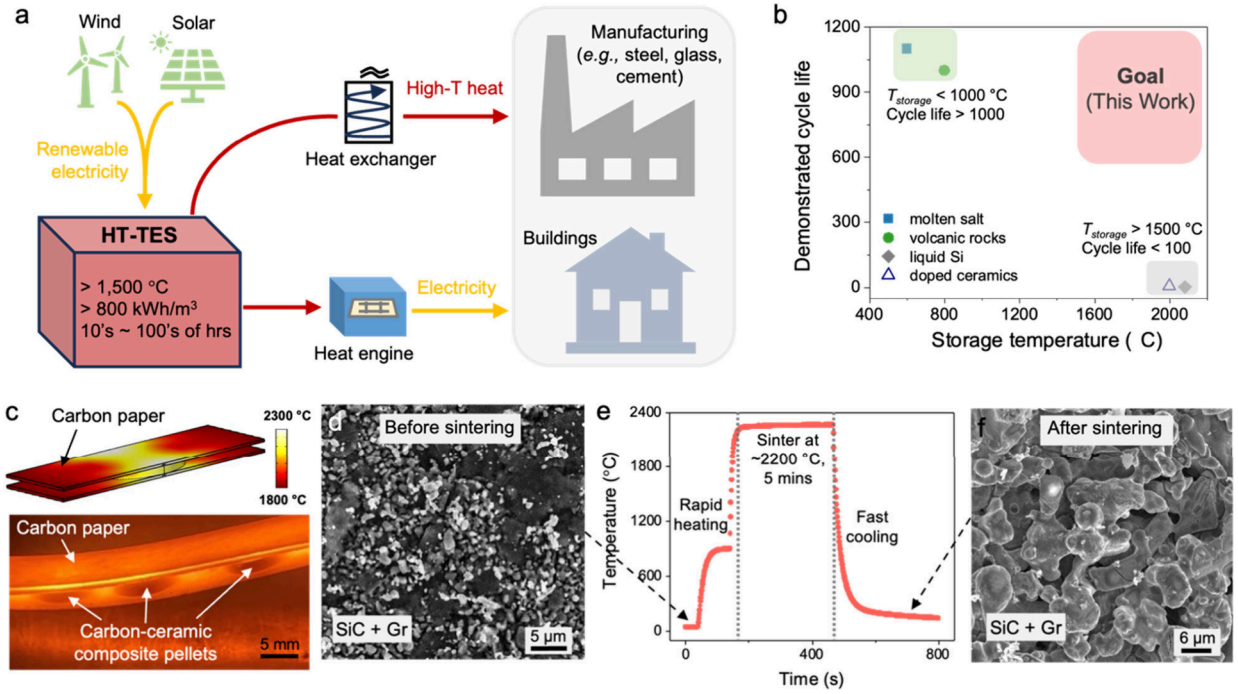

Figure 1. HT-TES system overview and storage material synthesis. (a) Overview schematic showing how HT-TES converts renewable electrical energy to high temperature thermal energy (>1500 °C) and supplies heat and electricity to the end-user. (b) Demonstrated cycle life of different thermal energy storage technologies[12,17,20,21] plotted versus their maximum storage temperature. Filled symbols represent storage materials that require separate indirect heaters, and empty symbols represent materials that can be directly resistance heated. Note that higher storage temperatures allow for larger energy storage densities. (c) Upper panel: modeled temperature profile using COMSOL during sintering of ceramic−graphite pellets with carbon paper as the heating element. Lower panel: a photograph of the sintering setup. (d and f) SEM micrograph of the SiC+Gr pellet (d) before and (f) after sintering. (e) Recorded temperature evolution of the carbon heater during the sintering process.

containment are still needed. Stand-alone solid ceramics and clays are inexpensive but require external heaters, which add to system complexity and reduce overall reliability. Recently, Stack et al. have addressed this issue by doping ceramics to make them electrically conductive, allowing for direct electrical self-heating.[17,18] However, their conductivity varies widely with temperature, making the material prone to thermal runaway during charging.[17] Pure graphite experiences thermal cycling fatigue as internal stresses accumulate from the anisotropic thermal expansion of separate grains, ultimately resulting in creep deformation and material failure.[19] Figure 1b summarizes the state of the art.[12,17,20,21] Currently, no stand-alone material in the literature satisfies all HT-TES requirements, leaving this critical need open (Supplementary Figure 1). To address this gap, we propose a class of ceramic−carbon composites with co-optimized thermal, electrical, and mechanical properties by controlling composition and microstructure using rapid sintering techniques.

Historically, the two most challenging HT-TES material properties to satisfy have been (i) rapid stable self-heating and (ii) cyclability. We therefore focus on creating these properties in simple ceramics as starting base materials that have otherwise desirable properties. Rapid stable self-heating requires a moderate level of electrical conductivity (~1,000 S/m) without a strong temperature dependence to avoid thermal runaway that would lead to heating instabilities.[17] We therefore chose graphite as a conductive filler to add to the ceramic matrix due to its overall weak temperature dependence resulting from its semimetal-like electronic band structure.[22] Like ceramics, graphite is also abundant, safe and remains solid at very high temperatures. We add enough graphite to exceed the percolation threshold (~33 vol %) based on the Bruggeman model (Supplementary Note 1). This ensures that enough distributed graphite can reliably form random continuous conductive pathways throughout the composite, giving it good electrical conductivity. It also enhances the composite's thermal conductivity, improving thermal stability and maximum block thickness as discussed later.

The composite also needs to withstand exposure to extreme spatial and temporal temperature gradients and survive repeated cycling of large temperature oscillations greater than 1,000 °C. While brittle materials with low Young's modulus and high tensile strength are resistant to thermal shock, they are highly susceptible to damage accumulation if thermal fracture does occur, resulting in catastrophic failure. In contrast, stiffer materials with lower tensile strength will fracture at smaller thermal strains but with less stored elastic energy, resulting in smaller and less devastating cracks.[23,24] To create an HT-TES material with both high thermal shock resistance and low damage accumulation, we manipulate the heterogeneous microstructure. The added graphite flakes serve a dual purpose and act like micromechanical thermal stress concentrators, nucleating a high density of uniformly distributed microcracks throughout the material when only a small amount of elastic energy has been accumulated.[23,25−27] These microcracks, along with the small but finite porosity, then act to volumetrically distribute absorption of the released elastic energy during fracture events so that no single crack grows large.[23,25,28] If thermal cycling causes sintering that closes cracks or pores, the graphite flakes ensure consistent

https://doi.org/10.1021/acsenergylett.4c03270
ACS Energy Lett. 2025, 10, 1002−1012

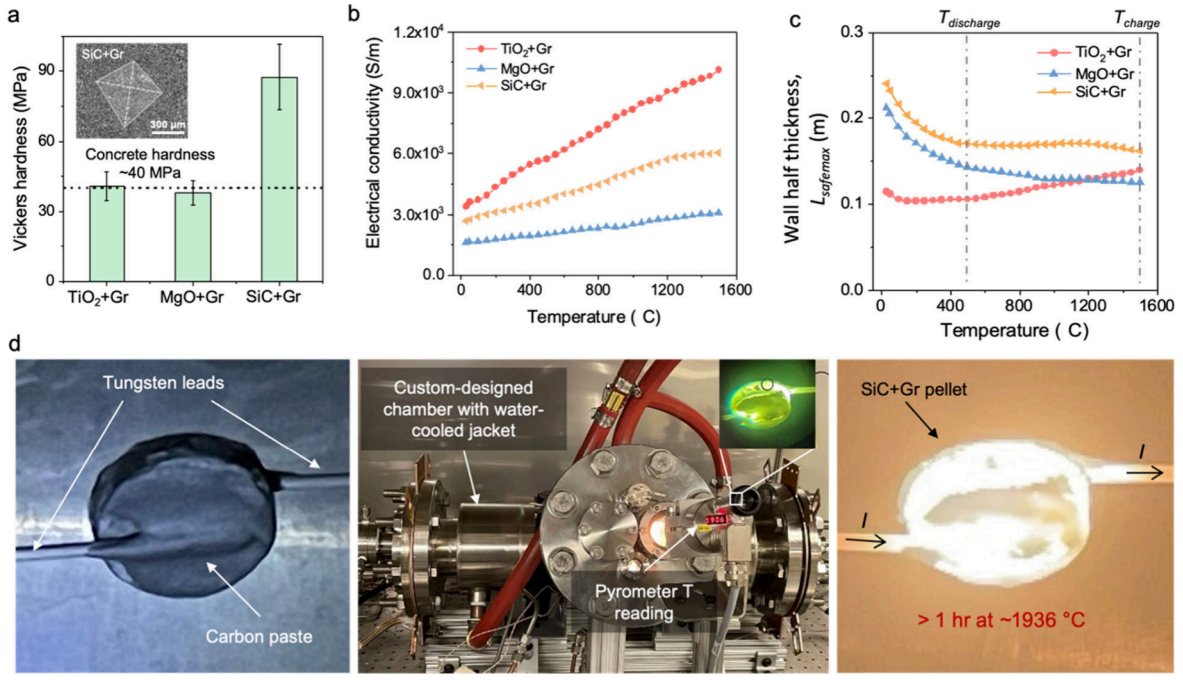

Figure 2. Rapid self-heating. (a) Measured Vickers hardness of all prepared pellets in this work, where the dashed line represents the measured hardness value of concrete for comparison.[30] Error bars represent measurement errors in the average length of the diagonal left by the indenter. (b) Measured temperature-dependent electrical conductivity of sintered composite pellets. (c) Maximum stable wall half thicknesses, $L_{safemax}$, as a function of temperature for different storage materials. HTF flow channel walls thinner than $2L_{safemax}$ will always dissipate hot spots and avoid thermal runaway (Supplementary Note 4). (d) Proof-of-concept demonstration. Direct resistance heating (DRH) of a SiC+Gr pellet to 1,936 °C for over an hour without any observed temperature instabilities or material degradations. Temperature is recorded using a pyrometer, and the test is conducted in an argon filled custom-designed chamber with a water-cooled jacket.

reforming of distributed microcracks in future cycling to limit the maximum crack size. The small ceramic grain sizes (~1 μm particle size) mean the comparatively large graphite flakes (~10 μm flake size) pin and deflect propagating cracks, further limiting damage accumulation.[24,26] The resulting composite can thus withstand exposure to extreme temperature gradients and many repeated thermal cycles without accumulating enough damage to significantly reduce its performance.

We individually evaluate TiO_2, MgO, and SiC as candidate composite matrix materials owing to these ceramics' high melting temperatures (>1800 °C), low cost, and chemical inertness. Pure ceramic powders are mixed with the graphite flakes, pressed into pellets, and sintered using an ultrafast high-temperature sintering (UHS) technique developed by Yao et al. (Figure 1c, details in Methods).[29] During sintering, the 100s of nm sized ceramic powder particles coalesce into grains of several microns in diameter (Figures 1d–f), while the graphite flakes do not sinter and retain their original tens of microns size. The average volumetric fill fraction increases from 48 ± 4% to 73 ± 2%, leaving a porosity low enough to preserve good energy density and thermal and electrical conductivities but high enough to help mitigate thermal cycling fatigue by acting as microcracks as discussed above. As indicated by X-ray photoelectron spectroscopy (XPS) results, the densification is achieved due to the additional chemical driving force beyond the normal capillary force using this UHS technique (Supplementary Figures 6–9, Supplementary Table 1).[29]

We quantified all HT-TES critical properties in the same samples and evaluated how these could impact the design of a full-scale system. All three composites satisfy HT-TES requirements with SiC+Gr exhibiting the best all-around performance, which we then subjected to more rigorous testing and investigations. Vickers hardness tests (Figure 2a, Methods) show that the composites all achieve a mechanical hardness comparable to or higher than that of concrete (40–50 MPa),[30] showing promise for structural TES blocks that can support their own weight. Heat capacity measurements and theoretical extrapolation to high temperatures confirm high energy densities in the range 0.87–1.03 MWh/m^3 (ΔT = 1000 °C, Supplementary Note 2). The thermal conductivities of the composites, κ, at room temperature are 2.9 W/m-K (TiO_2+Gr), 3.6 W/m-K (MgO+Gr), and 5.9 W/m-K (SiC +Gr) (Methods),[31] which are comparable to or better than various types of rocks successfully used in lower temperature TES studies such as granite (2.8 W/m-K), basalt (3.2 W/m-K), and hornfels (1.5 W/m-K).[32] Using an asymmetric effective medium Bruggeman's model, we extrapolate our measured room temperature thermal conductivity to 1,500 °C based on literature data for temperature dependencies of each component and considering the effects of interfacial thermal resistance (Supplementary Note 3).[33] Thermal conductivity also directly affects charging stability, as discussed below.

The electrical conductivities, σ, of the composites at room temperature are 3,382 S/m (TiO_2+Gr), 1,601 S/m (MgO +Gr), and 2,643 S/m (SiC+Gr), which are 10 to 100 times higher than the pure semiconductor ceramic components of TiO_2 (17.1 S/m) and SiC (362 S/m) and nearly 10,000 times higher than doped Cr_2O_3.[17] These values confirm the percolation threshold is achieved in all composites[34] (Methods, Supplementary Table 1). For a representative 800 MW direct-reduction iron plant,[35] 9,600 MWh of stored energy would be necessary to provide 12 h of continuous

https://doi.org/10.1021/acsenergylett.4c03270
ACS Energy Lett. 2025, 10, 1002–1012

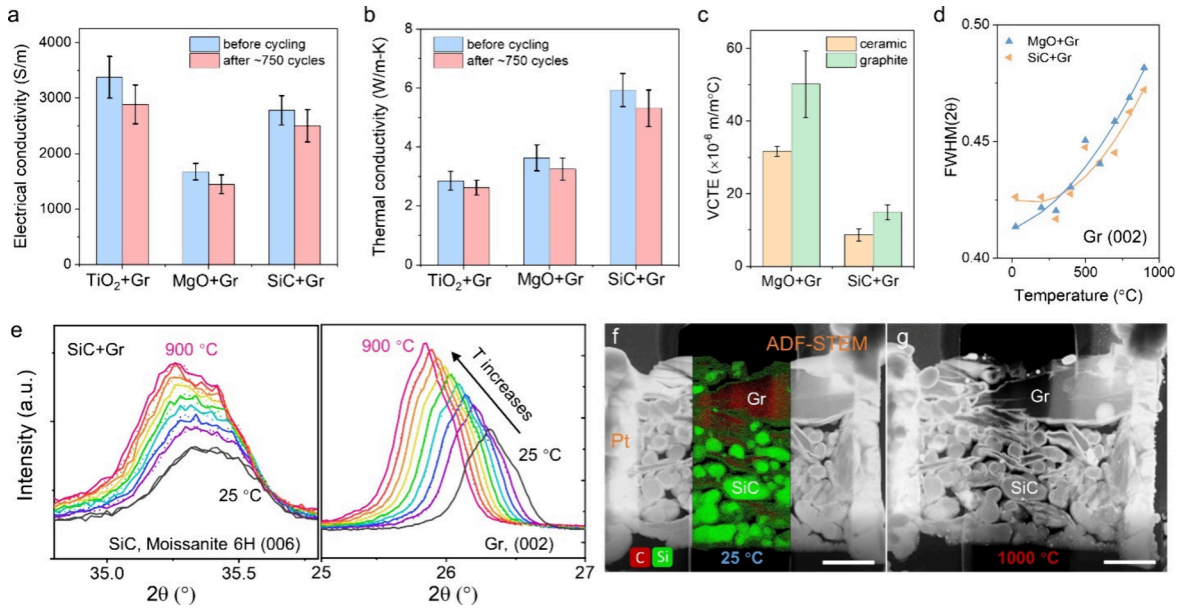

Figure 3. Thermal cycling fatigue resistance. (a) Measured room temperature electrical conductivity of the composite pellets before and after >753 thermal cycles (all with ~35% volume percentage of graphite). Error bars represent the uncertainties in pellet thickness measurements. (b) Measured room temperature thermal conductivity of the sintered pellets before and after >753 thermal cycles (all with ~35% volume percentage of graphite). Error bars represent the standard deviation of three hot disk measurements. (c) Measured average Volumetric Coefficient of Thermal Expansion (VCTE) for each phase within the composite pellets from 25 to 900 °C based on XRD results. Errors bars are mainly from the uncertainties in linear least-squares fitting. (d) Measured full width at half-maximum (fwhm) for the graphite (002) peak as a function of temperature within two different composites. Note that the lines are a guide for the eye. (e) Zoom-in XRD profiles of SiC +Gr composites showing the phase evolution as temperature increases from 25 to 900 °C. (f, g) Annular dark-field (ADF) scanning transmission electron microscopy (STEM) images showing a cross-section cut of the SiC+Gr sample at 25 and 1000 °C, respectively. The EDS mapping result is overlaid onto the STEM image to show each phase within the composite. Scale bar: 3 μm.

power. For these composites' electrical conductivities, such a system could be fully charged in 6 h using industrial charging voltages (Supplementary Figure 21), which could exploit the daily low-cost electricity window.

We also measure σ as a function of temperature up to operational HT-TES temperatures and confirm that all composites have a relative Temperature Coefficient of Conductivity (TCC) magnitude less than 0.01 K^{-1}, meaning that their electrical conductivity changes by less than 1% per degree change in temperature (Figure 2b). In contrast, HT-TES doped ceramics' relative TCC is ~1,000 times larger within the same temperature range.[17] TCC magnitude is critical for stability and safety during charging. If random fluctuations produce a hot spot during charging, a sufficiently large positive or negative TCC will cause local heat generation to intensify in a positive feedback loop, leading to thermal runaway and catastrophic failure (Supplementary Note 4). The TCC's sign determines whether such risk is associated with parallel or series current flow, both of which exist in 3D self-heated blocks. Our composites have a slight positive TCC, putting them at risk of failure in parallel configurations (Supplementary Figure 22). However, a small TCC can still be tolerated if heat passively conducts away from the hot spot faster than it is generated (Supplementary Note 4). Based on our composites' measured κ and TCC, we calculate the maximum allowable wall thickness between flow channels, $L_{safemax}$, below which heat will always conduct away fast enough to prevent thermal runaway for hot spots of any size (Figure 2c). For these composites, $L_{safemax}$ varies from 11 cm (TiO_2+Gr) to 17 cm (SiC+Gr) in the direction perpendicular to electrical current flow, enabling practical block geometries.[17]

To evaluate the practicality of the idea and demonstrate the self-heating capability, we developed a proof-of-concept device (Figure 2d). We performed a thermal soak-and-hold test by self-heating a SiC+Gr composite sample to 1,936 °C and holding it there for over an hour (Figure 2d, Methods), during which the sample did not exhibit any temperature instabilities or degradation.

To evaluate the thermal cycling stability of the composites, we measured σ and κ before and after thermally cycling each sample approximately 750 times (Figures 3a and b). Each cycle constituted ramping the sample up from 500 °C to 1,630 °C and back down again within 3 min (Supplementary Figures 24 and 25, details in Methods), creating spatial and temporal temperature gradients comparable to or greater than what would be experienced in a full-scale HT-TES system. Additionally, intermediate values of σ were measured every few 10s to 100s of cycles to track degradation (Supplementary Figure 26). Figures 3a and b show that all composites' transport properties remained stable within <14% throughout thermal cycling. This reduction primarily occurs during the first few cycles with little further degradation over the hundreds of remaining cycles tested (Supplementary Figure 26), indicating robust thermal cycling fatigue resistance and the potential to survive decades-long service life. We note that we also evaluated an Al_2O_3+Gr composite, but it experienced complete fracture failure during cycling, possibly due to a high temperature chemical reaction between alumina and graphite that produced trapped carbon monoxide gas,[36] building up pressure until failure.

To verify the microscopic mechanisms enabling this remarkable thermal stability, we perform high temperature X-

https://doi.org/10.1021/acsenergylett.4c03270
ACS Energy Lett. 2025, 10, 1002−1012

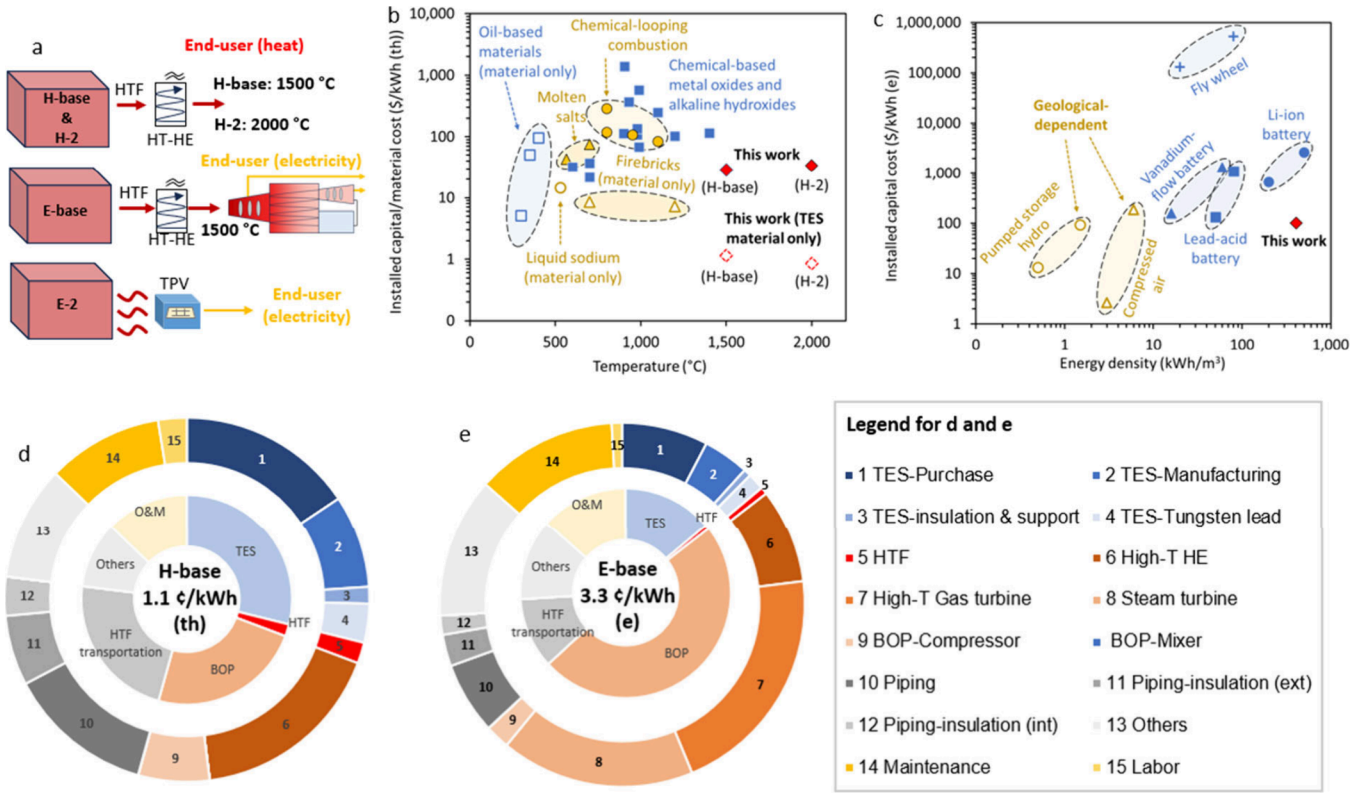

Figure 4. System cost evaluation. (a) High-level illustrations for applications evaluated in this study. "H" designates heat delivery under 1500 and 2000 °C for "H-base" and "H-2", respectively. "E" designates electricity delivery, where "E-base" uses heat exchangers coupled with CCGT and "E-2" uses TPV to convert the stored heat into electricity. "HTF" is heat transfer fluid, and "HT-HE" is a high-temperature heat exchanger. System sizes are 800 MW of heat or electricity delivery to the end-user, and the storage capacity is sized to provide corresponding power outputs for a duration of 12 h. (b) Comparison between this work and other heat storage methods from the literature based on the storage temperature and installed capital cost of the full system (filled in points) or of just the storage material (unfilled points). (c) Comparison between this work and other general energy storage methods from the literature based on the energy density and system installed capital cost. Unfilled points designate technologies that depend on specific geological features. Data for other studies are extracted from refs 8 and 41−43. Note that for heat storage we have included both material and system level data for other materials (where available). If not specified with "material only", capital costs for this work include all the components listed in Supplementary Note 5, other than O&M and others (i.e., installation and contingency). The energy density calculation in (c) for "this work" includes the volume of TES material, insulation, and support. The value for "this work" in (c) represents the E-base scenario. (d) Levelized cost of storage (LCOS) for the H-base scenario and its breakdown. (e) LCOS for the E-base scenario and its breakdown.

ray diffraction (XRD) from 25 to 900 °C on the SiC+Gr and MgO+Gr samples (Figures 3c−e, Methods). Chemical phase transition of the titania phase in the TiO_2+Gr sample complicated its XRD data analysis (confirmed by XPS measurements, Supplementary Figure 6). As discussed earlier, the graphite flakes function as micromechanical thermal stress concentrators to encourage the formation of a high density of uniformly distributed benign microcracks rather than fewer catastrophically large cracks during thermal fracture events. This stress concentration would necessitate thermal strain mismatches between the graphite and ceramic phases and would produce stress gradients within the graphite during heating. Both of these features are corroborated by the XRD data (Figures 3c−e). XRD measures the thermal expansion of each component within each composite from the temperature-dependent shift in its diffraction peak. We find the Volumetric Coefficient of Thermal Expansion (VCTE) of the graphite phase is indeed mismatched with that of the corresponding ceramic phase by roughly a factor of 2 in both samples (Figure 3c, more details in Supplementary Figure 30). We also measured the relative increase of the graphite phase diffraction peak widths with temperature to be on the order of 10^{-4} K^{-1} (tens of percent increases over cycling temperatures) (Figure 3d). Given the centimeter-sized X-ray spot size used and the tens of micron-sized graphite flakes, this diffraction peak broadening reveals increasingly heterogeneous strain in the graphite and hence thermal stress concentration from heating.[37]

While all composites satisfy all HT-TES requirements (Supplementary Table 1), SiC+Gr enables the largest and most stable storage blocks in a real system, making it the preferred composite for general HT-TES. We therefore performed high temperature in situ Transmission Electron Microscope (TEM) Videography on SiC+Gr to investigate the dynamic microstructural changes during heating from 25 to 1,000 °C (Figures 3f and g, Methods). The TEM videos confirmed that the existing pores and microcracks can accommodate significant thermal strain, preventing further crack propagation (Supplementary Videos 1−3).

Finally, we performed a techno-economic analysis (TEA) to assess the practical performance of a full-scale HT-TES system (enough storage to deliver 800 MW of heat or electricity to the end-user continuously for 12 h) based on the engineered composite materials in this work and the cost of balance of

https://doi.org/10.1021/acsenergylett.4c03270
ACS Energy Lett. 2025, 10, 1002−1012

plant such as heat exchangers, pipes, insulation, and heat engines. We conducted the TEA for two scenarios:

(1) Heat delivered at 1500 °C (Figure 4a): This temperature is applicable for blast furnaces, glass furnaces, steam methane reforming, and Carnot batteries for electricity using existing gas turbines. This scenario was chosen as components for balance of plant (BOP) already exist and are currently in use by the gas turbine industry.[38,39] In the published literature as shown in Figure 4b, no storage material exists even at 1500 °C. Chemical based metal oxides come close to this temperature but are significantly more expensive than our proposed material, and no reliable data on durability and thermal stability performance have been shown. Thus, the composites in this work could overcome one of the current barriers preventing HT-TES implementation. If the end use is heat, we refer to this as the H-base scenario, and if it is converted to electricity as end use, we call this the E-base scenario. For our generalized system, we use the design of conventional TES systems where temperature stratification is used to maintain high-temperature heat delivery during discharge.[32] Heat is efficiently conducted locally across flow path walls to the heat transfer fluid (HTF), while the system maintains a significant global temperature differential between the HTF inlets and exits.

(2) Heat delivered at 2000 °C (Figure 4a): We also speculatively evaluate the system's potential to deliver heat at 2000 °C (H-2 scenario) and convert that heat to electricity using thermophotovoltaics (TPVs) (E-2 scenario). TPVs are scalable solid-state heat engines capable of radiatively accepting >2000 °C heat without needing high temperature heat exchangers or heat transfer fluids. TPVs have been rapidly advancing in recent years and now possess heat-to-electricity conversion efficiencies of 40%.[40] These scenarios are more ambitious and rely on future R&D of the coupling infrastructures, and their costs and breakdowns are provided in Supplementary Figure 31.

For all scenarios (H-base, E-base, H-2, E-2), the modeled cost components (e.g., layered insulation material, heat transfer fluid) and economic parameters and assumptions are presented in Supplementary Note 5 and Supplementary Tables S3−S6. Figures 4b and c plot our system's projected upfront capital cost per unit energy stored for direct comparison with other energy storage technologies[8,41−43] as a function of output temperature (for heat output) and energy density (for electricity output). In addition to competitive cost and energy density, our material's ability to provide heat at such high temperatures can enable new opportunities for decarbonizing high emissions industries such as blast furnaces, glass, cement, and refractory metal (1500−2000 °C),[44−46] whose heat demands routinely exceed the operating temperature of conventional HT-TES such as molten salts (Figure 4b).

Figures 4d and e show the system levelized cost of storage (LCOS) and associated cost breakdown for the 1500 °C base cases of heat and electricity delivery. Based on the material performance experimentally demonstrated in this work, a theoretical full-scale HT-TES system could provide heat (H-base) at an LCOS of 1.1 ¢/kWh (th) and electricity (E-base) at 3.3 ¢/kWh (e), satisfying the Department of Energy's 2030 LCOS target of <5 ¢/kWh (e). LCOS calculations include material replacement based on cycle lifetime (included in annualized capital) and operation and maintenance (not including the charging cost), normalized to the annual energy output. The capital cost of the additional coupled system components (balance of plant) other than the HT-TES material collectively account for 49% of the LCOS for H-base and 61% for E-base. This includes components such as pipes, high-temperature heat exchangers (HT-HE), and combined cycle gas turbines (CCGT) for the E-base scenario. The 2000 °C scenarios could provide heat (H-2) at an LCOS of 1.2 ¢/kWh (th) and electricity (E-2) at 2.8 ¢/kWh (e), outperforming E-base. However, these scenarios still require further R&D on specific components (HT-HE for H-2 and TPV for E-2), as discussed in Supplementary Note 5. We project that capital costs of non-TES components would account for 55% of the total H-2 LCOS and 35% of E-2's LCOS (Supplementary Figure 31). Finally, our sensitivity analysis (Supplementary Figure 32) identifies the most important system parameters for deployment as high material stability (i.e., up to 750 cycles in this study), economical HT infrastructure (i.e., HT-HE for H-2 and CGGT for E-base), and high thermal-to-electrical heat engine conversion efficiency (for E-base and E-2). We note that, while our TEA assumes the experimentally demonstrated number of cycles (∼750), this number was limited by practical measurement constraints and not by sample degradation. We expect the composites would survive significantly more cycles if tested, further reducing LCOS by tens of percent for all scenarios. Lastly, although UHS provides important microstructural control and rapid synthesis, its commercial maturity level is still relatively low and its scalability is not yet proven. As noted in Supplementary Note 5, the manufacturing cost used in our TEA is analyzed primarily based on the energy consumption and assessments of commercially available sintering methods and not based on the UHS technique. Thus, future studies are encouraged to investigate higher technology readiness level (TRL) developments of this technique and its cost in greater detail.

We have presented microstructured ceramic−graphite composites as high temperature thermal energy storage materials that could help achieve full decarbonization by enabling societal electricity and heat demands to be powered using intermittent sources of renewable energy. These composites have been demonstrated to simultaneously satisfy all HT-TES material physical and economic requirements with SiC+Gr performing the best. Owing to their makeup and microstructure, these composites can survive prolonged high temperature exposure and rapid self-heating without thermal runaway and many hundreds of rapid thermal cycles from 500 °C to over 1,500 °C without degradation. They are made from safe, Earth-abundant, and inexpensive materials and could enable large scale energy storage at a price that makes 24/7 dispatchable renewable energy competitive with fossil fuels.

METHODS

Ultrafast High-Temperature Sintering (UHS) Using Carbon Heaters. The raw materials of ceramic powders (∼100−300 nm particle size, Sigma-Aldrich) and graphite flakes (∼5−10 μm flake size, Sigma-Aldrich) were first mixed with ball-milling, and the precursor powders were then pressed into pellets with a die using a hydraulic pressing tool (Carver, Inc. model 4120). The UHS was conducted in an argon filled chamber, and the heating rate and temperature of the Joule-heating carbon strip (Fuel Cell Earth) were precisely controlled by tuning the voltage of the power supply (Supplementary Figure 2).[29] The geometry of the carbon strips is designed to match the heater resistance with the

https://doi.org/10.1021/acsenergylett.4c03270
ACS Energy Lett. 2025, 10, 1002−1012

current and voltage limits of the power supply to achieve the ideal heating power and sintering temperature. Shown in Figure 1c, three pieces of carbon strips with carefully designed geometries are used as the heater for the sintering process, with three pressed pellets sandwiched between these heater strips being rapidly heated via thermal radiation and conduction. Using this method, a high heating rate of ~10^3 °C/min, a cooling rate up to ~5 × 10^3 °C/min, and a high sintering temperature of ~2,200 °C are achieved (Figure 1e). Similar to conventional spark plasma sintering, the ultrahigh heating rates of the UHS technique enhance the densification rate. The ultrafast sintering also minimizes cross-diffusion between the components to maintain the structural integrity, and the distinct phases forming the dense composite pellets are directly shown in the EDS elemental mapping of the sintered composite pellets (Supplementary Figures 10−12). The temperature of the heater is measured using a two-color pyrometer (Advanced Energy, Impac ISR 6 Advanced) with uncertainty of ±1 °C. The relative density of the sintered pellets is defined as 1-porosity, where the porosity is calculated based on the measured weight, volume, and the component intrinsic material density.

X-ray Photoelectron Spectroscopy (XPS) Characterization. The X-ray photoelectron spectroscopy (XPS) measurements were performed by using the Thermo-Fisher K-Alpha Plus XPS. The photon source was a monochromatized Al Kα line ($h\nu$ = 1486.6 eV). The spectra were acquired using a spot size of 400 μm. A flood gun with combined electrons and low energy Ar ions is used during the measurements. Based on the measured XPS spectrum before and after sintering, chemical state change was observed in the TiO_2+Gr composite (Supplementary Figure 6).

Energy Dispersive Spectroscopy (EDS) Measurements. The shape and size of features, surface topography, and chemistry of the composites were confirmed by a Field Emission Scanning Electron Microscope (FESEM, Zeiss Gemini Ultra55) coupled to a Bruker X-ray Energy Dispersive Spectrometer (X-ray EDS) used for identifying and mapping the distribution of chemical elements. EDS elemental mapping results for sintered composites are shown in Supplementary Figures 10−12.

Vickers Hardness Test. The mechanical hardness of the sintered pellets is measured using an Instron 5944 with a Vickers diamond tip. For this test, we first ramp up the indentation force to 10 N, hold for 10 s, and then retract the loading force from the sample surface (Supplementary Figure 13). The Vickers hardness is calculated based on the loading force and the measured indentation size. We performed the test at three different locations, and the calculated average value represents the sample hardness (Supplementary Figure 14). During the measurements, we make sure that the size of the hardness indentations (~40−500 μm) is much larger than the microstructural features of the composites (~200 nm−5 μm), and the measured results reflect the hardness of the composites as a whole.[47] Similar measurements have also been conducted on fine grained TiC/Ti_3AlC_2 particle composites with μm sized phases.[48]

Heat Capacity Measurements. The heat capacity was directly measured using differential scanning calorimetry (TA Instruments, DSC 2500) in hermetically sealed nonreacting anodized aluminum pans. The heat capacity measurements were calibrated using the NIST reference data for sapphire. We measured the heat capacity of all prepared pellets from 0 to 200 °C (Supplementary Figure 15).

Electrical Conductivity Measurements. The electrical conductivities of the sintered pellets are measured using the van der Pauw method. For the high temperature electrical conductivity measurements (up to 1,500 °C), high melting point tungsten wires (3,422 °C) are used as the electrical leads. In order to achieve stable electrical contact between the sample and the electrical leads, a custom-designed alumina sample holder is used, which consists of two alumina clamps and alumina screws, and the sample is sandwiched between the two clamps and tightened by four screws (Supplementary Figure 16). This measurement is performed in a high-temperature furnace in an argon environment with ±1 °C temperature control accuracy (MTI, GSL1700XS60). The van der Pauw method employs a four-point probe placed around the perimeter of the sample, which enables the measurement of an average resistivity of the sample through switching the current source and voltage probe leads. The average resistivity of a sample is given by $\rho = R_S t$, where the sheet resistance R_S is measured using the van der Pauw method and t is film thickness. Electrical conductivity measurements are conducted on three samples of each type to obtain an average value.

Cross-Plane Thermal Conductivity Measurements. The widely used hot disk transient plane source method (Hot Disk TPS 2200, Thermtest) is used to measure the room temperature thermal conductivity of the sintered pellets (Supplementary Figure 17). For this measurement, a thin metal foil disk (7577 sensor) with a bifilar spiral pattern is used as both the temperature sensor and the electrical resistive heater. The metal disk is sealed between two thin sheets of polyimide (Kapton), which act as a structural support and electrical insulator. In the experiment, the hot disk sensor is placed between two identical sintered composite pellets. A stepwise current is applied to the sensor, which generates a changing temperature in the sample and the sensor. By using resistance thermometry, the increase in the resistance of the metal sensor is measured over time to monitor the temperature increase in the sensor accurately (Supplementary Figure 18). The temperature response is analyzed to determine the thermal conductivity of the sample using a model developed for the idealized sensor with a known geometry, which serves as a boundary condition for the heat conduction problem in the sample.[31]

In-Plane Thermal Conductivity Measurements. The thermal conductivity was initially measured along the cross-plane direction using the hot disk method.[31] To further confirm the absence of thermal anisotropy within the as-prepared ceramic−graphite composites, we measured thermal conductivity of the same sample along the in-plane direction using the recently developed Structured Illumination with Thermal Imaging (SI-TI) platform in our group.[49] In brief, the SI-TI system is an optical pump−probe microscope that tolerates high surface roughness up to 3 μm and operates at low frequency (<10 Hz). This platform comprises an MTIR120 Thermal Imaging System from Microsanj and a visible light camera with infinity corrected optics. An Olympus LMPlanFL N 20×/0.40 objective lens is used to heat the sample and collect the thermoreflectance image. A Thorlabs M530L3 LED at 530 nm driven in the CW mode is used as probe light for thermoreflectance signal detection. The thermoreflectance signal is collected by a 1920 × 1200 pixel Si CMOS camera with 5.86 μm pitch size. A gold thin film

https://doi.org/10.1021/acsenergylett.4c03270
ACS Energy Lett. 2025, 10, 1002−1012

with thickness ∼70 nm is deposited on the sample surface for thermoreflectance imaging by the electron-beam physical vapor deposition method using the CHA Solution E-beam Evaporator.

As shown in Supplementary Figure 19, a simple rectangular heating pattern is used in the measurement and the phase difference between different regions of interest is used to avoid the characterization of the optical property of the Au layer and the absolute heating power.[49] The measurements of the SiC +Gr sample at multiple points provide a consistent in-plane thermal conductivity of 5.5 ± 0.5 W/m-K, which is consistent with the results from cross-plane thermal conductivity of 5.9 ± 0.4 W/m-K measured by hot disk. As such, we conclude that there is negligible anisotropy in the thermal conductivity for the sintered ceramic−carbon composites in this work.

Thermal Cycling Stability Test. For each thermal cycle, the pellet was placed into the carbon heater, heated from ∼500 to 1,630 °C, and then cooled down to 500 °C. The maximum temperature is intentionally chosen to be higher than the normal operating temperature of 1,500 °C to resemble a harsher working condition. For each cycle, the charging and discharging times are 92 and 88 s, respectively. These times are representative of full-scale system cycle times based on nondimensionalized scaling between laboratory sample sizes and full-scale system sizes. The details of the voltage settings and corresponding current of the power supply are shown in Supplementary Figure 24. After varying numbers of thermal cycles, we measured the electrical conductivity using the van der Pauw method and measured thermal conductivity using the hot disk method, both described above.

Direct Resistance Heating Test. High melting point tungsten wires are used as the electrical leads, and a thin layer of high-temperature carbon paste is applied at the connection between the tungsten leads and the pellet to spread the current (Figure 2d). We feed an ∼20 A DC current through the tungsten leads to the pellets producing high temperatures within the material via directly resistance heating. Pyrometer readings show a self-heating temperature of 1,936 °C. We hold the sample at high temperature for over an hour and do not observe any thermal instabilities or material degradation.

TEM Materials and Sample Preparation. The sintered composite samples were cleaved into ∼5 mm × 5 mm × 2 mm pieces with exposed flat faces for more practical TEM sample preparation. TEM foils were prepared using the lift-out process from the surface, where light to dark contrast indicated carbide/graphite or oxide/graphite interface (Supplementary Figure 27). Prior to FIB trenching and milling steps, a protective Pt layer was first deposited on the bulk sample surface using the electron beam (lower energy) and then a Pt layer was deposited using the Ga+ ion beam (Supplementary Figure 27). These Pt layers have been shown to be effective at minimizing beam damage to the surface of the sample by incident Ga+ ions. Moreover, the lift-out procedure used progressively lower beam current during each thinning step to ensure the sample was not affected before, during, and after lift-out and transfer to a Protochips Fusion Select MEMS device (SiN window). The lamella was carefully positioned over a milled section in the holey grid section of the observation window and welded in four corners without contacting the electrodes on either side. Final thinning and cleaning steps were performed on each side of the sample to remove most ion damage and contamination on the sample face produced by Ga+ and Pt exposure.

In Situ Heating and Nanodiffraction Electron Microscopy. In situ experimentation was conducted on a Thermofisher Scientific ThemIS image corrected microscope at 300 kV equipped with a Bruker SuperX energy dispersive X-ray spectroscopy (EDS) detector. The Bruker windowless detector allows for high count rates with minimal dead times and fast STEM-EDS mapping. The high speed Ceta2 camera can acquire 4k × 4k images at 40 frames per second for in situ movies. The Protochips biasing/heating holder is equipped with four electrical feedthroughs and can be tilted with a range of ±15° in alpha and ±8° in beta. The microscope is equipped with a support Fusion Select heating source and Axon software package, which allows for real-time heating and video for the duration of the in situ experiment. The electrothermal e-chip was tested via Fusion select software for a proper connection in the Protochips double tilt heating and biasing holder prior to the in situ experiment. The detected shift in peak temperature positions enables the measurement of relative temperatures. Furthermore, the electrothermal e-chip used in these experiments has been calibrated by Protochips to maintain 5% temperature accuracy and uniform heating across the entire heating membrane. The accuracy of this temperature measurement has been demonstrated to a statistical precision as low as 2.8 K. Similar MEMS-based electrothermal e-chips is well documented, and the error (±20 K) is not significantly affected by relative changes in temperature.[50] Moreover, there is a known temperature gradient across these types of devices; however, the probed sample regions are suspended over a single aperture, and it is assumed that the sample is only constrained by Pt welds fixing the lamella to the MEMS chip.

■ ASSOCIATED CONTENT

Data Availability Statement

The data that support the plots within this article and other findings of this study are available from the corresponding author upon request.

Supporting Information

The Supporting Information is available free of charge at https://pubs.acs.org/doi/10.1021/acsenergylett.4c03270.

Details of SEM images of composites before and after sintering, XPS spectrum and EDS mapping of the sintered composites, Vickers hardness measurements, measured volumetric heat capacity, electrical and thermal conductivity measurements, charging stability considerations, thermal cycling stability tests, in situ high temperature TEM and XRD examinations, and techno-economical analysis (TEA) (PDF)

TEM video 1, SiC+Gr composite under slow thermal cycling with Tmax = 750 °C (MP4)

TEM video 2, SiC+Gr composite subjected to a temperature ramp up to 960 °C (MP4)

TEM video 3, SiC+Gr composite exposed to a heating pulse reaching 1000 °C (MP4)

■ AUTHOR INFORMATION

Corresponding Authors

Sean Lubner − *Energy Storage and Distributed Resources Division, Lawrence Berkeley National Laboratory, Berkeley, California 94720, United States; Department of Mechanical Engineering, and Division of Materials Science and Engineering, Boston University, Boston, Massachusetts 02215,*

https://doi.org/10.1021/acsenergylett.4c03270
ACS Energy Lett. 2025, 10, 1002−1012

United States; orcid.org/0000-0002-8827-9688; Email: slubner@bu.edu

Hanna Breunig − *Energy Analysis and Environmental Impacts Division, Lawrence Berkeley National Laboratory, Berkeley, California 94720, United States;* orcid.org/0000-0002-4727-424X; Email: hannabreunig@lbl.gov

Ravi Prasher − *Energy Storage and Distributed Resources Division, Lawrence Berkeley National Laboratory, Berkeley, California 94720, United States; Department of Mechanical Engineering, University of California Berkeley, Berkeley, California 94720, United States;* orcid.org/0000-0002-3282-7147; Email: rsprasher@lbl.gov

Authors

Lin Yang − *Department of Advanced Manufacturing and Robotics, College of Engineering, Peking University, Beijing 100871, P. R. China; Energy Storage and Distributed Resources Division, Lawrence Berkeley National Laboratory, Berkeley, California 94720, United States;* orcid.org/0000-0003-4838-5213

Peng Peng − *State Key Laboratory of Mesoscience and Engineering, Institute of Process Engineering, Chinese Academy of Sciences, Beijing 100190, P. R. China; Energy Analysis and Environmental Impacts Division, Lawrence Berkeley National Laboratory, Berkeley, California 94720, United States;* orcid.org/0000-0001-6554-2247

Nathaniel Weger − *Energy Storage and Distributed Resources Division, Lawrence Berkeley National Laboratory, Berkeley, California 94720, United States; Department of Mechanical Engineering, University of California Berkeley, Berkeley, California 94720, United States;* orcid.org/0000-0002-5060-2590

Sean Mills − *Department of Materials Science and Engineering, University of California Berkeley, Berkeley, California 94720, United States; National Center for Electron Microscopy, Molecular Foundry, Lawrence Berkeley National Laboratory, Berkeley, California 94720, United States*

Clément Messeri − *Energy Storage and Distributed Resources Division, Lawrence Berkeley National Laboratory, Berkeley, California 94720, United States; Department of Materials Science and Engineering, University of California Berkeley, Berkeley, California 94720, United States*

Akanksha K. Menon − *Energy Storage and Distributed Resources Division, Lawrence Berkeley National Laboratory, Berkeley, California 94720, United States; George W. Woodruff School of Mechanical Engineering, Georgia Institute of Technology, Atlanta, Georgia 30332, United States;* orcid.org/0000-0003-1979-507X

Steven Zeltmann − *Department of Materials Science and Engineering, University of California Berkeley, Berkeley, California 94720, United States; National Center for Electron Microscopy, Molecular Foundry, Lawrence Berkeley National Laboratory, Berkeley, California 94720, United States*

Finn Babbe − *Chemical Sciences Division, Joint Center for Artificial Photosynthesis, Lawrence Berkeley National Laboratory, Berkeley, California 94720, United States;* orcid.org/0000-0002-9131-638X

Qiye Zheng − *Energy Storage and Distributed Resources Division, Lawrence Berkeley National Laboratory, Berkeley, California 94720, United States; Department of Mechanical Engineering, University of California Berkeley, Berkeley, California 94720, United States; Department of Mechanical and Aerospace Engineering, The Hong Kong University of Science and Technology, Hong Kong, SAR, China*

Chaochao Dun − *The Molecular Foundry, Lawrence Berkeley National Laboratory, Berkeley, California 94720, United States;* orcid.org/0000-0002-3215-6478

Chuan Zhang − *Insitute of Energy, Peking University, Beijing 100871, P. R. China;* orcid.org/0000-0001-8541-6029

Jeffrey J. Urban − *The Molecular Foundry, Lawrence Berkeley National Laboratory, Berkeley, California 94720, United States;* orcid.org/0000-0003-4909-2869

Andrew M. Minor − *Department of Materials Science and Engineering, University of California Berkeley, Berkeley, California 94720, United States; National Center for Electron Microscopy, Molecular Foundry, Lawrence Berkeley National Laboratory, Berkeley, California 94720, United States;* orcid.org/0000-0003-3606-8309

Complete contact information is available at: https://pubs.acs.org/10.1021/acsenergylett.4c03270

Author Contributions

[†]L.Y., P.P., N.W.: These authors contributed equally to this work. L.Y., N.W., A.K.M., and C.M. performed pellet preparation and sintering steps. L.Y. conducted Vickers hardness test and temperature dependent electrical conductivity measurements. C.D. performed XPS and EDS characterizations. Q.Z. conducted hot disk thermal conductivity measurements. L.Y. performed charging and discharging design calculations. L.Y. and N.W. conducted the direct resistance heating test. S.M., S.Z., F.B., and C.M. conducted XRD and in situ high temperature STEM tests. P.P. and H.B. performed technoeconomic analysis. L.Y., N.W., A.K.M., P.P., S.L., and R.P. compiled and analyzed results. L.Y., S.L., and R.P. wrote the manuscript. S.L., H.B., and R.P. directed the research.

Notes

The authors declare the following competing financial interest(s): S.L., R.P., L.Y., N.W., A.K.M., H.B., and P.P. are inventors on a US patent (patent pending) detailing the composite material fabrication, design, and operation for HT-TES. The rest of the authors declare no competing interests.

■ ACKNOWLEDGMENTS

This work was supported by the Laboratory Directed Research and Development (LDRD) Program of Lawrence Berkeley National Laboratory under U.S. Department of Energy Contract No. DE-AC02-05CH11231. This work was partially performed at the Molecular Foundry, Lawrence Berkeley National Laboratory, and was supported by the Department of Energy, Office of Science, Office of Basic Energy Sciences, Scientific User Facilities Division of the U.S. Department of Energy under Contract No. DE-AC02-05CH11231. S. Mills was supported by FUTURE (Fundamental Understanding of Transport Under Reactor Extremes), an Energy Frontier Research Center funded by the U.S. Department of Energy, Office of Science, Basic Energy Sciences. S. Zeltmann was supported by STROBE, a National Science Foundation STC funded under Grant No. DMR 1548924. The authors thank Dr. Vi Rapp for allowing them to use her lab space for some of the experiments in this work, including sintering, thermal cycling, and electrical conductivity measurement using a furnace. The authors also thank Antora Inc. and Electrified

https://doi.org/10.1021/acsenergylett.4c03270
ACS Energy Lett. 2025, 10, 1002−1012

Thermal Solutions Inc. for helpful discussions. We thank Rushabh Sailendra for helping with the pellet pressing steps. The authors thank Qin Yu and Jon Ell for training and allowing access to the Vickers hardness testing tool.

REFERENCES

(1) Lawrence Livermore National Laboratory and Department of Energy. *LLNL Flow Charts*. Department of Energy. https://flowcharts.llnl.gov/ (accessed January 2, 2022).
(2) Chen, H.; Cong, T. N.; Yang, W.; Tan, C.; Li, Y.; Ding, Y. Progress in Electrical Energy Storage System: A Critical Review. *Progress in Natural Science* **2009**, *19* (3), 291−312.
(3) Schmidt, O.; Hawkes, A.; Gambhir, A.; Staffell, I. The Future Cost of Electrical Energy Storage Based on Experience Rates. *Nature Energy 2017 2:8* **2017**, *2* (8), 1−8.
(4) Ziegler, M. S.; Mueller, J. M.; Pereira, G. D.; Song, J.; Ferrara, M.; Chiang, Y. M.; Trancik, J. E. Storage Requirements and Costs of Shaping Renewable Energy Toward Grid Decarbonization. *Joule* **2019**, *3* (9), 2134−2153.
(5) Sandalow, D.; Friedmann, J.; Aines, R.; McCormick, C.; McCoy, S.; Stolaroff, J. *ICEF Industrial Heat Decarbonization Roadmap - CDR Law*. https://cdrlaw.org/resources/icef-industrial-heat-decarbonization-roadmap/ (accessed April 23, 2022).
(6) Gilbert, T.; Menon, A. K.; Dames, C.; Prasher, R. Heat Source and Application-Dependent Levelized Cost of Decarbonized Heat. *Joule* **2023**, *7* (1), 128−149.
(7) Dumont, O.; Frate, G. F.; Pillai, A.; Lecompte, S.; De paepe, M.; Lemort, V. Carnot Battery Technology: A State-of-the-Art Review. *J. Energy Storage* **2020**, *32*, 101756.
(8) Fernandes, D.; Pitié, F.; Cáceres, G.; Baeyens, J. Thermal Energy Storage: "How Previous Findings Determine Current Research Priorities. *Energy* **2012**, *39* (1), 246−257.
(9) Lubner, S. D.; Prasher, R. S. Combined Heat and Electricity Using Thermal Storage to Decarbonize Buildings and Industries. *One Earth* **2022**, *5* (3), 230−231.
(10) Henry, A.; Prasher, R.; Majumdar, A. Five Thermal Energy Grand Challenges for Decarbonization. *Nat. Energy* **2020**, *5* (9), 635−637.
(11) Woods, J.; Mahvi, A.; Goyal, A.; Kozubal, E.; Odukomaiya, A.; Jackson, R. Rate Capability and Ragone Plots for Phase Change Thermal Energy Storage. *Nat. Energy* **2021**, *6* (3), 295−302.
(12) Amy, C.; Pishahang, M.; Kelsall, C.; LaPotin, A.; Brankovic, S.; Yee, S.; Henry, A. Thermal Energy Grid Storage: Liquid Containment and Pumping above 2000 °C. *Appl. Energy* **2022**, *308*, 118081.
(13) Amy, C.; Budenstein, D.; Bagepalli, M.; England, D.; Deangelis, F.; Wilk, G.; Jarrett, C.; Kelsall, C.; Hirschey, J.; Wen, H.; Chavan, A.; Gilleland, B.; Yuan, C.; Chueh, W. C.; Sandhage, K. H.; Kawajiri, Y.; Henry, A. Pumping Liquid Metal at High Temperatures up to 1,673 K. *Nature* **2017**, *550* (7675), 199−203.
(14) Polkowski, W.; Sobczak, N.; Nowak, R.; Kudyba, A.; Bruzda, G.; Polkowska, A.; Homa, M.; Turalska, P.; Tangstad, M.; Safarian, J.; Moosavi-Khoonsari, E.; Datas, A. Wetting Behavior and Reactivity of Molten Silicon with H-BN Substrate at Ultrahigh Temperatures up to 1750 °C. *J. Mater. Eng. Perform* **2018**, *27* (10), 5040−5053.
(15) Polkowski, W.; Sobczak, N.; Bruzda, G.; Kudyba, A.; Nowak, R.; Polkowska, A.; Krzak, I.; Tchórz, A.; Giuranno, D. Silicon-Boron Alloys as New Ultra-High Temperature Phase-Change Materials: Solid/Liquid State Interaction with the h-BN Composite. *Silicon* **2020**, *12* (7), 1639−1649.
(16) Polkowski, W.; Sobczak, N.; Nowak, R.; Bruzda, G.; Kudyba, A.; Polkowska, A.; Krzak, I.; Tchórz, A. Solid/Liquid Interaction between Si-Based Phase Change Materials and Refractories. *Ultra-High Temperature Thermal Energy Storage, Transfer and Conversion* **2021**, 113−137.
(17) Stack, D. C. Development of High-Temperature Firebrick Resistance-Heated Energy Storage (FIRES) Using Doped Ceramic Heating System. Ph.D. thesis; MIT, 2021.
(18) Stack, D. C.; Curtis, D.; Forsberg, C. Performance of Firebrick Resistance-Heated Energy Storage for Industrial Heat Applications and Round-Trip Electricity Storage. *Appl. Energy* **2019**, *242*, 782−796.
(19) Jenkins, G. M.; Williamson, G. K. Deformation of Graphite by Thermal Cycling. *J. Appl. Phys.* **1963**, *34* (9), 2837−2841.
(20) Malta Inc. https://www.maltainc.com/ (accessed January 2, 2022).
(21) Forsberg, C.; Aljefri, A. S. 100-Gigawatt-Hour Crushed-Rock Heat Storage for Concentrated Solar Power and Nuclear. *Solar-Paces2020* **2022**, *2445*, 160006.
(22) Iwashita, N.; Imagawa, H.; Nishiumi, W. Variation of Temperature Dependence of Electrical Resistivity with Crystal Structure of Artificial Graphite Products. *Carbon N Y* **2013**, *61*, 602−608.
(23) Hasselman, D. P. H. Thermal Stress Resistance of Engineering Ceramics. *Materials Science and Engineering* **1985**, *71*, 251−264.
(24) Fairbanks, C. J.; Lee, H. L.; Haselman, D. P. H. Effect of Crystallites on Thermal Shock Resistance of Cordierite Glass-Ceramics. *J. Am. Ceram. Soc.* **1984**, *67* (11), c236−c237.
(25) Hasselman, D. P. H. Unified Theory of Thermal Shock Fracture Initiation and Crack Propagation in Brittle Ceramics. *J. Am. Ceram. Soc.* **1969**, *52* (11), 600−604.
(26) Morena, R.; Niihara, K.; Haselman, D. P. H. Effect of Crystallites on Surface Damage and Fracture Behavior of a Glass-Ceramic. *J. Am. Ceram. Soc.* **1983**, *66* (10), 673−682.
(27) Hasselman, D. P. H. Griffith Criterion and Thermal Shock Resistance of Single-Phase Versus Multiphase Brittle Ceramics. *J. Am. Ceram. Soc.* **1969**, *52* (5), 288−289.
(28) Kriegel, W. W.; Palmour, H., III. Ceramics in Severe Environments. In *Proceedings of the Sixth University Conference on Ceramic Science*; Springer Nature: Raleigh, NC, 1970; pp 1−601.
(29) Yao, Y.; Huang, Z.; Xie, P.; Lacey, S. D.; Jacob, R. J.; Xie, H.; Chen, F.; Nie, A.; Pu, T.; Rehwoldt, M.; Yu, D.; Zachariah, M. R.; Wang, C.; Shahbazian-Yassar, R.; Li, J.; Hu, L. Carbothermal Shock Synthesis of High-Entropy-Alloy Nanoparticles. *Science (1979)* **2018**, *359*, 1489−1494.
(30) Hou, P.; Zhang, R.; Cheng, X. Case Study of the Gradient Features of in Situ Concrete. *Case Studies in Construction Materials* **2014**, *1*, 154−163.
(31) Zheng, Q.; Kaur, S.; Dames, C.; Prasher, R. S. Analysis and Improvement of the Hot Disk Transient Plane Source Method for Low Thermal Conductivity Materials. *Int. J. Heat Mass Transf* **2020**, *151*, 119331.
(32) Alva, G.; Lin, Y.; Fang, G. An Overview of Thermal Energy Storage Systems. *Energy* **2018**, *144*, 341−378.
(33) Nan, C.-W.; Birringer, R.; Clarke, D. R.; Gleiter, H. Effective Thermal Conductivity of Particulate Composites with Interfacial Thermal Resistance. *J. Appl. Phys.* **1997**, *81* (10), 6692.
(34) Wang, B. X.; Zhou, L. P.; Peng, X. F. A Fractal Model for Predicting the Effective Thermal Conductivity of Liquid with Suspension of Nanoparticles. *Int. J. Heat Mass Transf* **2003**, *46* (14), 2665−2672.
(35) 2021 World Direct Reduction Statistics. https://www.midrex.com/wp-content/uploads/MidrexSTATSBook2021.pdf (accessed January 23, 2025).
(36) Balomenos, E.; Panias, D.; Paspaliaris, I.; Friedrich, B.; Jaroni, B.; Steinfeld, A.; Guglielmini, E.; Halmann, M.; Epstein, M.; Vishnevsky Eth-Zürich, I. Carbothermic Reduction of Alumina: A Review of Developed Processes and Novel Concepts. *Proceedings of EMC* **2011**, 729−743.
(37) Vashista, M.; Paul, S. Correlation between Full Width at Half Maximum (FWHM) of XRD Peak with Residual Stress on Ground Surfaces. *Philos. Mag.* **2012**, *92* (33), 4194−4204.
(38) Shiozaki, S.; Fujii, T.; Takenaga, K.; Ozawa, M.; Yamada, A. Gas Turbine Combined Cycle. *Advances in Power Boilers*; Elsevier: 2021; pp 305−344. DOI: 10.1016/B978-0-12-820360-6.00006-0.
(39) Colmenar-Santos, A.; Gómez-Camazón, D.; Rosales-Asensio, E.; Blanes-Peiró, J. J. Technological Improvements in Energetic

Efficiency and Sustainability in Existing Combined-Cycle Gas Turbine (CCGT) Power Plants. *Appl. Energy* **2018**, *223*, 30−51.
(40) LaPotin, A.; Schulte, K. L.; Steiner, M. A.; Buznitsky, K.; Kelsall, C. C.; Friedman, D. J.; Tervo, E. J.; France, R. M.; Young, M. R.; Rohskopf, A.; Verma, S.; Wang, E. N.; Henry, A. Thermophotovoltaic Efficiency of 40%. *Nature* **2022**, *604* (7905), 287−291.
(41) Viswanathan, V.; Mongird, K.; Franks, R.; Li, X.; Sprenkle, V.; Baxter, R. *2022 Grid Energy Storage Technology Cost and Performance Assessment*; 2022.
(42) Zhang, H.; Baeyens, J.; Cáceres, G.; Degrève, J.; Lv, Y. Thermal Energy Storage: Recent Developments and Practical Aspects. *Prog. Energy Combust. Sci.* **2016**, *53*, 1−40.
(43) Bayon, A.; Bader, R.; Jafarian, M.; Fedunik-Hofman, L.; Sun, Y.; Hinkley, J.; Miller, S.; Lipiński, W. Techno-Economic Assessment of Solid-Gas Thermochemical Energy Storage Systems for Solar Thermal Power Applications. *Energy* **2018**, *149*, 473−484.
(44) Lakhdar, Y.; Tuck, C.; Binner, J.; Terry, A.; Goodridge, R. Additive Manufacturing of Advanced Ceramic Materials. *Prog. Mater. Sci.* **2021**, *116*, 100736.
(45) McMillan, C. A.; Ruth, M. Using Facility-Level Emissions Data to Estimate the Technical Potential of Alternative Thermal Sources to Meet Industrial Heat Demand. *Appl. Energy* **2019**, *239*, 1077−1090.
(46) Guo, Z.; Zhang, J.; Zong, Y.; Xiao, Z.; Wang, C.; Zhu, W.; Zhang, Y.; Jiao, K. Physicochemical Properties of Cinder and Alkaline Modification in Tuyere Birdnest Region of Blast Furnace. *Fuel* **2023**, *348*, 128595.
(47) Shi, Y.; Neubrand, A.; Koch, D. Characterization of Hardness and Stiffness of Ceramic Matrix Composites through Instrumented Indentation Test. *Adv. Eng. Mater.* **2019**, *21* (5), 1800806.
(48) Ruan, M. M.; Feng, X. M.; Ai, T. T.; Yu, N.; Hua, K. Microstructure and Mechanical Properties of TiC/Ti3AlC2 In Situ Composites Prepared by Hot Pressing Method. *Mater. Sci. Forum* **2015**, *816*, 200−204.
(49) Zheng, Q.; Chalise, D.; Jia, M.; Zeng, Y.; Zeng, M.; Saeidi-Javash, M.; Tanvir, A. N. M.; Uahengo, G.; Kaur, S.; Garay, J. E.; Luo, T.; Zhang, Y.; Prasher, R. S.; Dames, C. Structured Illumination with Thermal Imaging (SI-TI): A Dynamically Reconfigurable Metrology for Parallelized Thermal Transport Characterization. *Appl. Phys. Rev.* **2022**, *9* (2), No. 021411.
(50) Niekiel, F.; Kraschewski, S. M.; Müller, J.; Butz, B.; Spiecker, E. Local Temperature Measurement in TEM by Parallel Beam Electron Diffraction. *Ultramicroscopy* **2017**, *176*, 161−169.

https://doi.org/10.1021/acsenergylett.4c03270
ACS Energy Lett. 2025, 10, 1002−1012